

**Modeling flow of Carreau fluids in porous media**Christopher A. Bowers<sup>1</sup> and Cass T. Miller<sup>1</sup>*Department of Environmental Sciences and Engineering, University of North Carolina at Chapel Hill, North Carolina 27599, USA* (Received 29 January 2023; accepted 4 November 2023; published 11 December 2023)

Carreau fluids occur routinely in porous medium systems for a range of applications, and the dependence of the viscosity for such fluids on the rate of strain tensor poses challenges to modeling at an averaged macroscale. Traditional approaches for macroscale modeling such flows have relied upon experimental observations of flows for generalized Newtonian fluids (GNFs) and a phenomenological approach referred to herein as the shift factor. A recently developed approach based upon averaging conservation and thermodynamic equations from the microscale for Cross model GNFs is extended to the case of Carreau fluids and shown to predict the flow through both isotropic and anisotropic media accurately without the need for GNF-flow experiments. The model is formulated in terms of rheological properties, a standard Newtonian resistance tensor, and a length-scale tensor, which does require estimation. An approach based upon measures of the morphology and topology of the pore space is developed to approximate this length-scale tensor. Thus, this work provides the missing components needed to predict Carreau GNF macroscale flow with only rheological information for the fluid and analysis of the pore morphology and topology independent of any fluid flow experiments. Accuracy of predictions based upon this approach is quantified, and extension to other GNFs is straightforward.

DOI: [10.1103/PhysRevE.108.065106](https://doi.org/10.1103/PhysRevE.108.065106)**I. INTRODUCTION**

Non-Newtonian fluids appear frequently in natural and engineered systems, including geological flows [1–8], biological flow in the body [9–14], and subsurface industrial processes [14–24]. The prevalence and complexity of non-Newtonian fluids has led to a proliferation of modeling approaches in the literature [14,18,21,23,25–31], with no one approach being universally accepted [21,26,27,31]. This complexity includes shear rate dependence and thixotropic behavior, as well as viscoelasticity [14,23,26,32–34], which have been observed to be important in some porous medium systems [14,21,23–27,31,35].

Fluids for which the dynamic viscosity depends upon the instantaneous shear rate, temperature, and pressure but not explicitly on time are called generalized Newtonian fluids (GNFs), and these are often present in flows in porous medium systems [18,23,24,26,35,36]. GNFs exhibit a stress-strain relationship such that

$$\boldsymbol{\tau}_w = 2\hat{\mu}_w(\dot{\boldsymbol{\gamma}}_w)\mathbf{d}_w, \quad (1)$$

where  $\boldsymbol{\tau}_w$  is the viscous stress tensor for an incompressible fluid,  $\hat{\mu}_w$  is the dynamic viscosity, which is dependent on the shear rate  $\dot{\boldsymbol{\gamma}}_w$ ,  $\mathbf{d}_w$  is the symmetric rate of strain tensor, and the subscript  $w$  indicates that these quantities apply to the fluid phase at the microscale, also called the pore scale [26,32,34,35,37]. GNFs exhibit complex shear profiles in porous media that can change dramatically with flow rate, which has complicated their modeling at both the microscale and the macroscale, which is a continuum scale in which

averaging is performed over a representative elementary volume consisting of many pores [14,24,26,27,31,35,36]. The macroscale is sometimes referred to as the porous medium continuum scale, and it is a length scale relied upon to solve many applications of interest. The details of the pore morphology and topology resolved at the microscale are lost at the macroscale and replaced with extent measures such as volume fractions and specific interfacial areas.

Typically, GNFs are simulated in porous medium systems at the macroscale by using models developed for Newtonian fluids and empirically fitting an effective viscosity at each flow rate [18,21,24,27,35,36]. This approach requires fitting a shift factor for each medium and fluid of interest. Additionally, the calculation of the shear rate in Eq. (1) is numerically complex [38–40] and has led to computational methods that either rely on simplified analogs, such as pore network models [21,23,24,24–26,29,30,41–44], or are incapable of simulating realistically sized systems [36]. An ideal macroscale model for GNFs would be able to simulate flow through a medium using known properties of the medium and rheological characteristics of the fluid, without the need to run experiments for each GNF and medium of interest.

Among GNFs, Cross [18,27,29,30,35,36] and Carreau [14,21,24,26–28,31] model fluids are two of the most prevalent, especially in subsurface processes such as hydraulic fracturing. A macroscale model has been proposed for Cross model fluids that does not require observed data for every GNF of interest [35]; however, such a model has not been formulated for Carreau fluids, and the Cross model approach relies upon the determination of a length-scale tensor that may not be easily accessible. Extension of this model to Carreau fluids as well as a method of estimating the length-scale tensor based on properties of the medium are important open issues.

\*bowersca@live.unc.edu

The goal of this work is to develop and validate a macroscale model for Carreau fluids flowing in single-fluid porous medium systems. The specific objectives are (1) to develop a macroscale model for Carreau fluids that relies upon only rheological characterization of fluid properties and accessible porous medium properties, (2) to validate the macroscale model for a variety of porous medium systems and fluid properties, and (3) to develop an approach to estimate the length-scale tensor used in macroscale modeling of GNFs.

## II. BACKGROUND

### A. Microscale modeling of Carreau fluids

Carreau model fluids exhibit a viscosity-shear rate dependence given by

$$\hat{\mu}_w(\dot{\gamma}_w) = \hat{\mu}_\infty + (\hat{\mu}_0 - \hat{\mu}_\infty)[1 + (\hat{\lambda}\dot{\gamma}_w)^2]^{\frac{n-1}{2}}, \quad (2)$$

where  $\hat{\mu}_\infty$  is the viscosity as the shear rate approaches infinity,  $\hat{\mu}_0$  is the viscosity at zero shear rate,  $\hat{\lambda}$  is a relaxation time, and  $n$  is a non-Newtonian power index [26,34]. The shear rate is

$$\dot{\gamma}_w = \sqrt{2\mathbf{d}_w:\mathbf{d}_w}, \quad (3)$$

and the rate of strain tensor,  $\mathbf{d}_w$ , is [34,37]

$$\mathbf{d}_w = \frac{1}{2}[\nabla\mathbf{v}_w + (\nabla\mathbf{v}_w)^T], \quad (4)$$

where  $\mathbf{v}_w$  is the microscale fluid velocity vector.

It is often the case that simplified rheological models are selected instead of the Carreau model, such as rheological power laws within constrained shear rate cases, or power law with cutoff (PLCO) approaches [45], which are both often restricted to shear-thinning fluids. However, rheological power laws have been found to poorly model real systems that span a wide range of shear rates [46–48], and PLCO approaches do not accurately model the rheology of fluids that are transitioning from a Newtonian plateau to power-law behavior, and vice versa. To ensure that models are accurate across the full range of shear rates that are expected in many porous medium systems, four-parameter rheological models deserve consideration. The shear rates of concern for a given system are in turn related to the range of flow rates exhibited.

In addition to simplified rheological models, GNFs have often been modeled at the microscale using simplified geometric approximations, such as a bundle of capillary tubes or other pore-network models [21,23–26,29,30,41–44]. While these models have proven computationally efficient, they do not accurately represent the complex morphology and topology of many porous media, making them suboptimal [49–51]. Lattice Boltzmann methods (LBMs) have been used to model GNFs at the microscale [52–56], and a three-dimensional LBM has been used to simulate Cross model fluids but not Carreau model fluids [36]. OpenFOAM, an open-source simulation toolkit, has also been used to simulate GNFs at the microscale, including Carreau model fluids [14,18,36]. Microscale simulations are often carried out to inform macroscale models based on a shift-factor approach to enable the simulation of systems at lengths scales that are not accessible with microscale simulation alone [18,21,27,36,57–60].

### B. Shift-factor approach

The shift-factor approach, although this terminology is not universally used to describe this method, has been the predominant approach used for macroscale modeling of GNFs in porous medium systems. The shift factor is based on applying Darcy's law to non-Newtonian fluids, as well as Newtonian fluids by introducing an effective viscosity [18,21,24,25,27,35,36,42,43,61–66]. Darcy's law can be written for a Newtonian fluid as

$$\mathbf{q}^{\bar{\bar{w}}} = -\frac{\hat{\mathbf{k}}^w}{\hat{\mu}^w} \cdot (\nabla p^w - \rho^w \mathbf{g}^{\bar{\bar{w}}}), \quad (5)$$

where  $\mathbf{q}^{\bar{\bar{w}}}$  is the volumetric flux for the system, often called the Darcy velocity,  $\hat{\mathbf{k}}^w$  is the intrinsic permeability tensor,  $\hat{\mu}^w$  is the macroscale dynamic viscosity of the fluid,  $p^w$  is the fluid pressure,  $\rho^w$  is the fluid density,  $\mathbf{g}^{\bar{\bar{w}}}$  is the gravitational acceleration vector, superscripts indicate macroscale quantities, and double overbars indicate a quantity that is defined as a specific average of microscale quantities [37,67–72]. For the shift-factor approach,  $\hat{\mu}^w$  in Eq. (5) is replaced by an effective viscosity,  $\mu_{\text{eff}}^{\bar{\bar{w}}}$ , which is calculated using an effective shear rate,  $\dot{\gamma}_{\text{eff}}^{\bar{\bar{w}}}$ , defined for an isotropic system by

$$\dot{\gamma}_{\text{eff}}^{\bar{\bar{w}}} = \hat{\alpha} \frac{q^{\bar{\bar{w}}}}{\sqrt{\epsilon^{\bar{\bar{w}}} \hat{k}^w}}, \quad (6)$$

where  $\hat{\alpha}$  is the shift factor,  $q^{\bar{\bar{w}}}$  is the magnitude of the Darcy velocity,  $\epsilon^{\bar{\bar{w}}}$  is the porosity of the system, and  $\hat{k}^w$  is the isotropic intrinsic permeability. Eq. (6) is a dimensionally consistent scaling ansatz that relates the effective shear rate to the volumetric flux and medium properties.

The shift-factor approach is typically used for isotropic systems [18,21,24,27,36], with few anisotropic examples in the literature [57–60]. There is disagreement in the literature whether the shift factor depends upon the fluid or not [35,36]. The shift-factor approach requires fitting  $\hat{\alpha}$  for simulation or experimental flow data for each GNF of interest flowing through the medium of interest after Newtonian characterization of  $\hat{k}^w$  [35]. This is more complicated than the way that Newtonian fluid flow is modeled, which is often approximated based on surrogate measures of the pore morphology and topology to predict  $\hat{k}^w$  and Darcy's law [67,68]. Additionally, many porous media are anisotropic, making them inappropriate for the shift factor approach as it has been typically written [18,21,24,27,36].

### C. Averaging theory approach

Thermodynamically constrained averaging theory (TCAT) is a hierarchical model building approach that uses microscale conservation and thermodynamic principles to develop closed models at a variety of length scales that can involve fluid flow, species and energy transport, and reactions [37,70,73]. TCAT modeling hierarchies have been developed and applied to many phenomena that occur in porous medium systems, including single-fluid flow [37,69,74–76], two-fluid flow [37,77–79], tumor growth [80–82], and single GNF flow porous medium systems [35], as well as sediment transport [83].

Bowers and Miller [35] used TCAT to derive a macroscale model for the flow of a single-phase Cross model fluid through porous media. This model was capable of simulating flow of Cross model fluids in porous media without needing to calculate a shift factor so long as a characteristic length-scale tensor,  $\hat{\mathbf{L}}^w$ , was accessible.  $\hat{\mathbf{L}}^w$  was calculated from

$$-(2\hat{\mu}_w \mathbf{d}_w \cdot \mathbf{n}_w)_{\Omega_{ws}, \Omega_{ws}} = \hat{\mathbf{L}}^w \cdot \hat{\mathbf{R}}^w \cdot \mathbf{v}^{\bar{w}}, \quad (7)$$

where  $\mathbf{n}_w$  is the surface normal of the  $w$  phase,  $\hat{\mathbf{R}}^w$  is a symmetric second-rank resistance tensor,  $\mathbf{v}^{\bar{w}}$  is the density weighted average velocity, and  $\langle \cdot \rangle_{\Omega_{ws}, \Omega_{ws}}$  is an averaging operator evaluated over the fluid-solid, or  $ws$ , interface [35,37]. The general form of the averaging operator is described in the literature and accommodates many different types of averages arising in the theory. The subscripts specify the regions of integration and normalization, respectively. An independent expression involving  $\hat{\mathbf{R}}^w$  is available based upon an entropy inequality that ensures agreement with the second law of thermodynamics. For a Newtonian fluid,  $\hat{\mathbf{R}}^w$  may be related to  $\hat{\mathbf{k}}^w$  by [35, Eq. (41)]

$$\frac{\hat{\mathbf{k}}^w}{\hat{\mu}^w} = \epsilon^{\bar{w}^2} (\hat{\mathbf{R}}^w)^{-1}, \quad (8)$$

providing a connection between the TCAT analysis and Darcy's law.

It was also shown that

$$|-(2\hat{\mu}_w \mathbf{d}_w \cdot \mathbf{n}_w)_{\Omega_{ws}, \Omega_{ws}}| = \hat{\mu}_{\text{eff}}^{\bar{w}} \dot{\gamma}_{\text{eff}}^{\bar{w}}, \quad (9)$$

linking an effective viscosity and shear rate to averaged microscale quantities [35].

Eq. (7) may be used to calculate  $\hat{\mathbf{L}}^w$  for a Newtonian fluid and applied to model GNFs when microscale simulation data are available [35]. Because  $\hat{\mathbf{L}}^w$  was found to be a property of the medium, we posit that this tensor can be approximated based upon surrogate measures of the morphology and topology of the pore structure. If this is so, a GNF-flow model can be developed and applied using only standard Newtonian characterization of a medium and the rheological properties of the fluid.

### III. MACROSCALE MODEL

#### A. Formulation approach

The purpose of this section is to formulate a macroscale model based upon averaging from the microscale and thermodynamically constrained closure relations that are consistent with the second law of thermodynamics [37,70,73]. This approach provides a connection between the microscale and macroscale that results in a precise description of all macroscale quantities and enables the use of microscale simulations to evaluate approximations made to close the macroscale model. The phenomenon of concern is single fluid flow of a Carreau fluid through a porous medium system represented at the macroscale. The TCAT approach will be used to derive a Carreau model for flow through a porous medium of focus in this work.

A model that incorporates GNF rheology may be derived by applying secondary restrictions specific to our use case

to the general TCAT model hierarchy for single-fluid flow through porous media available in the literature [37]. The secondary restrictions applied here are the same as those applied in [35]: (1) the system is isothermal; (2) both phases are of a constant composition in space and time with no mass transfer; (3) the interface between the fluid and solid phase is massless; (4) the solid phase is immobile and incompressible, with a constant volume fraction in space and time; (5) the fluid flow is in the Stokes regime and inertial terms in the momentum equation are unimportant; and (6) the fluid is incompressible, of constant density at the microscale and macroscale, and with a viscosity that depends only upon the instantaneous shear rate, i.e., a GNF without temperature or pressure effects. The sections that follow summarize the components of the proposed model.

#### B. Conservation equations

A macroscale model for the restricted single-fluid phase system of concern includes a conservation of mass equation of the form [37, Eq. (6.73)]

$$\frac{\partial(\epsilon^{\bar{w}} \rho^w)}{\partial t} + \nabla \cdot (\epsilon^{\bar{w}} \rho^w \mathbf{v}^{\bar{w}}) = 0, \quad (10)$$

and a conservation of momentum equation that can be written as [37, Eq. (6.92)]

$$\begin{aligned} \frac{\partial(\epsilon^{\bar{w}} \rho^w \mathbf{v}^{\bar{w}})}{\partial t} + \nabla \cdot (\epsilon^{\bar{w}} \rho^w \mathbf{v}^{\bar{w}} \mathbf{v}^{\bar{w}}) - \nabla \cdot (\epsilon^{\bar{w}} \mathbf{t}^{\bar{w}}) \\ - \epsilon^{\bar{w}} \rho^w \mathbf{g}^{\bar{w}} - \overset{s \rightarrow w}{\mathbf{T}} = \mathbf{0}, \end{aligned} \quad (11)$$

where  $t$  is time,  $\mathbf{t}^{\bar{w}}$  is the stress tensor, and  $\overset{s \rightarrow w}{\mathbf{T}}$  is the rate of momentum density transfer from the solid phase to the fluid phase. Producing a solvable model based on Eqs. (10) and (11) requires closure approximations for  $\mathbf{t}^{\bar{w}}$  and  $\overset{s \rightarrow w}{\mathbf{T}}$ , which must be consistent with the second law of thermodynamics. This consistency condition is expressed as a simplified entropy inequality [37, Eq. (9.63)].

#### C. Closure approximations

The simplified entropy inequality can be used to deduce a zero-order approximation for the stress tensor, which can be written as [35, Eq. (19)]

$$\mathbf{t}^{\bar{w}} = -p^w \mathbf{I}, \quad (12)$$

where  $\mathbf{I}$  is the identity tensor. Eq. (12) can be interpreted as an approximation that the macroscale stress tensor is inviscid, which follows from the dominant role of the interphase transfer of momentum between the fluid phase and the surface of the solid phase internal to the domain, which is represented separately and denoted  $\overset{s \rightarrow w}{\mathbf{T}}$  [35,37].

An approximation is also needed for  $\overset{s \rightarrow w}{\mathbf{T}}$ , which may be deduced from a first-order, conjugate flux-force approximation based upon the simplified entropy inequality as [35, Eq. (20)]

$$\epsilon^{\bar{w}} \nabla p^w - \epsilon^{\bar{w}} \rho^w \nabla(\mu^{\bar{w}} + \psi^{\bar{w}}) - \epsilon^{\bar{w}} \rho^w \mathbf{g}^{\bar{w}} - \overset{s \rightarrow w}{\mathbf{T}} = \hat{\mathbf{R}}^w \cdot \mathbf{v}^{\bar{w}}, \quad (13)$$

where  $\mu^{\bar{w}}$  is the chemical potential, and  $\psi^{\bar{w}}$  is the gravitational potential.

For the GNF of focus in this work, it is useful to equate  $\hat{\mathbf{R}}^w$  to the fluid viscosity and the known dependence on the rate of strain tensor. Because the macroscale equations have been derived by averaging from the microscale, the averaged definition of  $\overset{s \rightarrow w}{\mathbf{T}}$  can be substituted into Eq. (13), simplifications can be made based on secondary restrictions, and the desired relationship deduced as [35, Eq. (28)]

$$\begin{aligned} & \epsilon^{\bar{w}s} \langle \rho_w \psi_w \mathbf{n}_w \rangle_{\Omega_{ws}, \Omega_{ws}} + \epsilon^{\bar{w}s} \langle p_w \mathbf{n}_w \rangle_{\Omega_{ws}, \Omega_{ws}} \\ & - \epsilon^{\bar{w}s} \langle 2\hat{\mu}_w \mathbf{d}_w \cdot \mathbf{n}_w \rangle_{\Omega_{ws}, \Omega_{ws}} = \hat{\mathbf{R}}^w \cdot \mathbf{v}^{\bar{w}}, \end{aligned} \quad (14)$$

where  $\epsilon^{\bar{w}s}$  is the specific interfacial area of the  $ws$  interface between the solid and fluid phases.

#### D. Carreau fluid resistance tensor

The purpose of this section is to formulate an expression for  $\hat{\mathbf{R}}^w$  for the case of a Carreau GNF. Inspired by the success in modeling Cross model fluids at the macroscale [35], we posit a functional form for  $\hat{\mathbf{R}}^w$  that is similar to the microscale Carreau model for viscosity given by Eq. (2), which may be written as

$$\hat{R}_{ii}^w(q_i^{\bar{w}}) = \hat{R}_{ii}^w + (\hat{R}_{ii}^w - \hat{R}_{ii}^w) [1 + (\hat{\Lambda}_i q_i^{\bar{w}})^2]^{\frac{n-1}{2}}, \quad (15)$$

where  $\hat{R}_{ii}^w$  is the Newtonian resistance at the infinite shear rate viscosity,  $\hat{R}_{ii}^w$  is the Newtonian resistance at the zero shear rate viscosity,  $\hat{\Lambda}_i$  is a constant related to  $\hat{\lambda}$ ,  $i$ 's are indexes specifying a vector or tensor component, and  $\hat{\mathbf{R}}^w$  is assumed to be diagonal as a result of the principal directions of the medium being oriented with the Cartesian coordinate directions.  $\hat{R}_{ii}^w$  and  $\hat{R}_{ii}^w$  may be calculated from Eq. (8), where the viscosity is replaced by the corresponding Newtonian viscosity limits from the Carreau fluid model.

The unknown coefficients  $\hat{\Lambda}_i$  must be computed. Because of the posited similarity in scaling of  $\hat{\mu}_w$  and  $\hat{\mathbf{R}}^w$ , a reference point is chosen such that

$$\hat{\mu}_r = \sqrt{\hat{\mu}_0 \hat{\mu}_\infty} \quad (16)$$

and

$$\hat{R}_{ir}^w = \sqrt{\hat{R}_{ii}^w \hat{R}_{ii}^w}, \quad (17)$$

where the subscript  $r$  denotes the reference point. Because the scaling between the Newtonian limits in Eqs. (2) and (15) is due to the quantities within brackets in each equation, we may equate these quantities at the reference velocity and solve for  $\hat{\Lambda}_i$  giving

$$\hat{\Lambda}_i = \frac{\hat{\lambda} \dot{\gamma}_r}{q_{ir}^{\bar{w}}}, \quad (18)$$

where  $\dot{\gamma}_r$  is the reference shear rate at which  $\hat{\mu}_r$  occurs, which can be computed from Eq. (2). To solve for  $\hat{\Lambda}_i$ ,  $q_{ir}^{\bar{w}}$  must be determined, which can be accomplished using Eqs. (7) and (9), recalling that

$$q_i^{\bar{w}} = \epsilon^{\bar{w}} v_i^{\bar{w}}, \quad (19)$$

evaluating for the reference conditions in each direction giving

$$q_{ir}^{\bar{w}} = \frac{\epsilon^{\bar{w}} \sqrt{\hat{\mu}_0 \hat{\mu}_\infty} \dot{\gamma}_r}{\hat{L}_{ii}^w \sqrt{\hat{R}_{ii}^w \hat{R}_{ii}^w}}. \quad (20)$$

Substituting Eq. (20) into Eq. (18) gives

$$\hat{\Lambda}_i = \frac{\hat{\lambda} \hat{L}_{ii}^w \sqrt{\hat{R}_{ii}^w \hat{R}_{ii}^w}}{\epsilon^{\bar{w}} \sqrt{\hat{\mu}_0 \hat{\mu}_\infty}}. \quad (21)$$

Eqs. (15) and (21) may be used to calculate a resistance for Carreau model fluids without the need to carry out experiments or simulations beyond those needed to compute  $\hat{\mathbf{R}}^w$  and  $\hat{\mathbf{L}}^w$ , which are accessible for a Newtonian fluid. Estimation of these two tensors from surrogate measures of the system properties could further reduce the data burdens needed to model GNF flow through porous medium systems.

#### E. Carreau fluid resistance profile

The Carreau fluid resistance model profile transitions between constant Newtonian limits at both low and high values of the shear rate, which follows from the functional form given by Eq. (15). To evaluate the flow rate range over which significant deviation from Newtonian behavior is expected, Eq. (15) can be differentiated with respect to  $q_i^{\bar{w}}$  yielding

$$\frac{\partial \hat{R}_{ii}^w}{\partial q_i^{\bar{w}}} = (\hat{R}_{ii}^w - \hat{R}_{ii}^w) \hat{\Lambda}_i^2 (n-1) q_i^{\bar{w}} \left[ 1 + (\hat{\Lambda}_i q_i^{\bar{w}})^2 \right]^{\frac{n-3}{2}}. \quad (22)$$

Evaluating Eq. (22) as a function of  $q_i^{\bar{w}}$  provides a measure of the deviation from Newtonian behavior. At the limits of low and high shear rates, this equation tends toward zero, while markedly nonzero over the transition region between these two limits.

## IV. METHODS

### A. Overview

Section III advanced a macroscale model for the flow of a Carreau fluid through a porous medium system. This model was based upon a posited scaling behavior and an extension to a previously validated macroscale model for Cross model fluids. The existing validated Cross model [35] and the posited Carreau GNF macroscale model both include a length-scale tensor  $\hat{\mathbf{L}}^w$  that must be determined. Because the macroscale model is based upon averaging microscale equations to the macroscale, all macroscale quantities are described in terms of averages of microscale quantities, which provides opportunities for model evaluation and validation. To take advantage of these opportunities, microscale simulations of a range of systems were relied upon to evaluate and validate the proposed model, and to advance an approach to estimate the needed parameters. The range of media and fluid properties, microscale computational approach, model evaluation and validation methods, and parameter estimation approach used are summarized in turn in the sections that follow.

TABLE I. Carreau model fluid parameters.

| Parameter                     | Fluid 1              | Fluid 2              | Fluid 3              | Fluid 4              |
|-------------------------------|----------------------|----------------------|----------------------|----------------------|
| $\hat{\mu}_0$ (Pa s)          | $1.0 \times 10^0$    | $1.0 \times 10^1$    | $1.0 \times 10^0$    | $1.0 \times 10^0$    |
| $\hat{\mu}_\infty$ (Pa s)     | $1.0 \times 10^{-2}$ | $1.0 \times 10^{-2}$ | $1.0 \times 10^{-2}$ | $1.0 \times 10^{-2}$ |
| $\hat{\lambda}$ (s)           | $1.0 \times 10^4$    | $1.0 \times 10^4$    | $1.0 \times 10^5$    | $1.0 \times 10^4$    |
| $n$                           | $7.0 \times 10^{-1}$ | $7.0 \times 10^{-1}$ | $7.0 \times 10^{-1}$ | $5.0 \times 10^{-1}$ |
| $\rho^w$ (kg/m <sup>3</sup> ) | $1.0 \times 10^3$    | $1.0 \times 10^3$    | $1.0 \times 10^3$    | $1.0 \times 10^3$    |

**B. System properties**

Several different porous medium systems were selected for model validation and parameter estimation as summarized in Table II. The media considered were a body-centered cubic array of spheres (BCC), a body-centered array of ellipsoids (BCE), random sphere packs consisting of 25 and 1000 spheres, and random ellipsoid packs. The BCC system was selected as a unit test, being simple enough to simulate at high resolution, while generating flow paths that are more complex than what is seen in a capillary system. The BCE system provides an anisotropic unit test similar to the BCC system and was generated by stretching the BCC system until a target ellipsoid aspect ratio of 2 was reached. The 1000 random sphere systems were used to evaluate results generated from the small random sphere packs. The random sphere packs were made up of nonoverlapping spheres whose radii were log-normally distributed, generated using an available method [84].

To develop approximations of  $\hat{\mathbf{L}}^w$ , a set of 1000 25-sphere systems was developed that spanned a wide range of pore structures. Simulations were carried out using randomly packed spheres, packed using the same methods as the 1000 sphere systems described above. Isotropic packings were generated with log-normal variances in sphere radii of 0, 0.01, 0.05, 0.1, and 0.5. For each targeted radii variance, packings were generated with porosities of 0.36, 0.38, 0.4, 0.42, and 0.44, and for each targeted porosity 20 packings were generated, giving a total of 500 systems. The anisotropic system packings were generated by packing an isotropic system in a domain that was noncubic, and then stretching this domain into a cubic domain, turning the spheres into ellipsoids. Systems were stretched in one dimension by an amount that would give the target aspect ratio for each ellipsoid. Anisotropic domains were generated with aspect ratios of 2,

2.5, 3, 3.5, and 4, and for each aspect ratio packings were generated with porosities of 0.36, 0.38, 0.4, 0.42, and 0.44, giving a set of 500 anisotropic systems, which all consisted of identical monodispersed particles. For both the isotropic and anisotropic system sets, the mean radius was allowed to change to accommodate the targeted porosity, log-normal variance, and system dimensions, and the nondimensional interpretation of the results made this scaling inconsequential. A set of sphere packings consisting of 1000 spheres were generated to validate the model to approximate  $\hat{\mathbf{L}}^w$ . These packings were generated with a porosity of 0.4, and had log-normal variance in sphere radii of 0, 0.01, 0.05, 0.1, 0.5, with two systems being generated for each variance. System properties are summarized in Table II, and example systems are shown in Fig. 1.

All simulations consisted of single fluid flow of a Newtonian or Carreau fluid through a porous medium. For simulations meant to validate the macroscale model, four different Carreau fluids were considered, with parameters listed in Table I. The fluids, and flow conditions, were selected to ensure a wide range of GNF behavior while maintaining Stokes flow. For the estimation of  $\hat{\mathbf{L}}^w$  each simulation consisted of a Newtonian fluid flowing through a medium with  $\hat{\mu}_w = 1.0 \times 10^{-3}$  Pa s and  $\rho_w = 1.0 \times 10^3$  kg/m<sup>3</sup>. Carreau model fluid flow was simulated for one 1000-sphere packing with log-normal variance of 0 in order to compare the resistance predicted using the estimated value of  $\hat{\mathbf{L}}^w$  to the observed resistance.

**C. Computational approach**

Microscale simulations have been found to be a useful tool when studying macroscale phenomena, especially when macroscale models are directly derived from microscale models as was done here [35–37]. Microscale simulations were

TABLE II. Porous media properties.<sup>a</sup>

| Parameter                                | BCC                          | BCE                          | RPSI                | RPE                 | RPSII              |
|--|------------------------------|------------------------------|---------------------|---------------------|--------------------|
| Length in $x$ (m) <sup>b</sup>           | $1 \times 10^{-3}$           | $1 \times 10^{-3}$           | $1 \times 10^{-5}$  | $1 \times 10^{-5}$  | $1 \times 10^{-5}$ |
| Number of spheres/ellipsoids             | 2                            | 2                            | 25                  | 25                  | 1000               |
| Porosity, $\epsilon^{\bar{w}}$           | 0.325                        | 0.325                        | 0.36–0.44           | 0.36–0.44           | 0.4                |
| Log-normal mean radius (m) <sup>bc</sup> | $0.433012702 \times 10^{-3}$ | $0.433012702 \times 10^{-3}$ | —                   | —                   | —                  |
| Log-normal variance                      | 0                            | 0                            | 0–0.5               | 0                   | 0–0.5              |
| Number of background cells               | $8 \times 10^6$              | $1.6 \times 10^7$            | $3.375 \times 10^6$ | $3.375 \times 10^6$ | $1.25 \times 10^8$ |
| Number of systems analyzed               | 1                            | 1                            | 500                 | 500                 | 10                 |

<sup>a</sup>Randomly packed spheres are RPS, randomly packed ellipsoids are RPE. RPSI is a 25 sphere system, RPSII is a 1000-sphere system.

<sup>b</sup>The BCE system includes one dimension which is double the other two dimensions, as described in Sec. IV B.

<sup>c</sup>For RPS and RPE systems, log-normal mean radii were allowed to vary so that other medium properties could be defined at runtime.

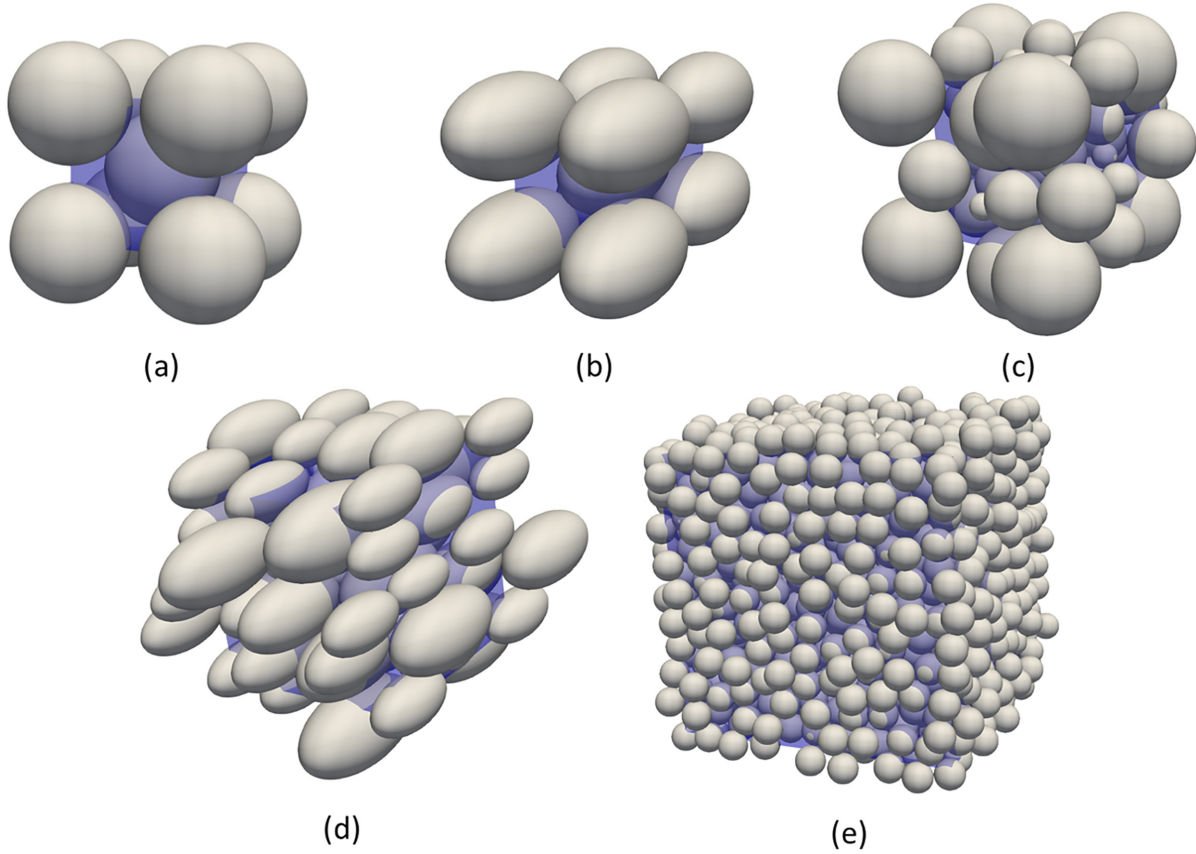


FIG. 1. Porous medium systems used: (a) a BCC array of spheres; (b) a BCE array of ellipsoids; (c) random sphere packs with 25 spheres; (d) random ellipsoid packs with 25 ellipsoids; and (e) random sphere packs with 1000 spheres. In all figures the blue box represents the domain.

used here both to validate the proposed macroscale model as well as to develop a data set to evaluate approximations for  $\hat{\mathbf{L}}^w$ . Simulations were conducted using OpenFOAM, an open-source modeling toolkit that has been found to be useful in non-Newtonian studies [18,35,36]. Simulations were composed of a mesh generation step, followed by a flow simulation. At run time, averaged microscale quantities were calculated using functions built into OpenFOAM [85].

For each system a mesh was generated at the microscale using the blockMesh and snappyHexMesh utilities that are built into OpenFOAM [85]. All cases were meshed using near-solid refinement to improve model accuracy at the fluid-solid interface similarly to other studies [35,86]. All boundaries of the system were periodic. The size of each mesh was selected such that computational error would be insignificant. The adequate mesh refinement was determined by simulating a wide range of flow rates for fluid 4 through increasingly refined systems. With each level of refinement, the hydraulic resistance was calculated using Eq. (14), and the Richardson extrapolation for the hydraulic resistance was calculated using data from different refinements. For two refinement levels  $m_1$  and  $m_2$ , which correspond here to cell refinement in a single dimension, Richardson's extrapolation may be used to give an estimate of the numerically converged resistance,  $\hat{\mathbf{R}}^{w*}$ , by

$$\hat{\mathbf{R}}^{w*} = \frac{(m_1/m_2)^n \hat{\mathbf{R}}_{m_2}^w - \hat{\mathbf{R}}_{m_1}^w}{(m_1/m_2)^n - 1}, \quad (23)$$

where  $\hat{\mathbf{R}}_{m_2}^w$  and  $\hat{\mathbf{R}}_{m_1}^w$  are the resistances observed at refinements  $m_1$  and  $m_2$  respectively, and  $n$  is the order of numerical convergence, which is approximately second order for such systems [87]. Once the relative error between the observed and the extrapolated resistance was less than 1%, the system was considered grid independent. The number of cells used in the background mesh that achieved grid independence is listed in Table II.

OpenFOAM flow simulations were performed using the simpleFOAM solver, which supports Carreau fluids [85,88]. SimpleFOAM solves the incompressible mass and momentum balance equations

$$\nabla \cdot \mathbf{v}_w = 0, \quad (24)$$

$$\nabla \cdot (\mathbf{v}_w \mathbf{v}_w) - \nabla \cdot \boldsymbol{\tau}_w = -\nabla p_w + \mathbf{S}, \quad (25)$$

where  $\mathbf{S}$  is a momentum source term. The viscous stress tensor was calculated using Eq. (1), the rate of strain tensor was calculated from Eq. (4), and the shear rate was calculated from Eq. (3). The viscosity followed a Carreau model using Eq. (2), and flow was driven by imposing a body force  $\mathbf{S}$ . For isotropic systems, the body force was directed in one dimension only. For anisotropic systems, each simulation was carried out with a body force directed in one dimension, with separate simulations performed for flow in each of the principal directions of the medium. The SIMPLE algorithm was carried out by simpleFOAM, and linear systems of algebraic

equations were solved using the geometric algebraic multigrid (GAMG) solver [85] with a specified relative error tolerance of 1E-8.

#### D. Evaluation and validation

The macroscale model proposed herein was evaluated for a range of systems to determine its accuracy and range of applicability. The systems evaluated were summarized in Sec. IV B. Model evaluation was done by integrating microscale simulation results and determining  $\hat{R}_{ii}^w$  using Eq. (14),  $\hat{L}_{ii}^w$  using Eq. (7), and  $\hat{k}_{ii}^w$  using Eq. (8)—all for Stokes flow of a Newtonian fluid. These parameters, the rheological properties of the fluids, and Eqs. (15) and (18) were used to predict the observed Stokes flow of GNFs and compare to values of  $\hat{R}_{ii}^w$  determined from microscale simulation data for every medium, Carreau fluid, and flow condition computed by the direct application of Eq. (14) to the simulated GNF flow data.

#### E. Length-scale tensor approximation

The GNF model for a Carreau fluid includes a length-scale tensor,  $\hat{\mathbf{L}}^w$ , as shown in Eq. (21). This tensor can be computed using Eq. (7) if microscale simulation or experimental data is available for Stokes flow of a Newtonian fluid. Estimation of  $\hat{\mathbf{L}}^w$  based upon more readily available surrogate measures was undertaken to evaluate the extent to which approximate methods can enable simpler application of the GNF flow model derived. The set of candidate variables upon which to base an approximation of  $\hat{\mathbf{L}}^w$  was

$$\mathcal{V} = \{\epsilon^{\bar{w}}, \epsilon^{\bar{ws}}, \epsilon^{\bar{ws}} J_w^{ws}, \epsilon^{\bar{ws}} K_w^{ws}, \hat{\mathbf{R}}_0^w, \mathbf{S}_2^{\bar{w}}\}, \quad (26)$$

where  $J_w^{ws}$  is the mean curvature of the  $ws$  interface,  $K_w^{ws}$  is the Gaussian curvature of the  $ws$  interface, and  $\mathbf{S}_2^{\bar{w}}$  is a vector two-point correlation measure of the pore structure. The variables from this set denoted  $\epsilon^{\bar{w}}$ ,  $\epsilon^{\bar{ws}}$ ,  $\epsilon^{\bar{ws}} J_w^{ws}$ , and  $\epsilon^{\bar{ws}} K_w^{ws}$  are normalized forms of the set of Minkowski functionals known from integral geometry to be important descriptors for sets of positive reach, which have been shown useful for describing the state of porous medium systems [89–93].

The two-point correlation provides the probability that two points selected within the medium are within the same phase as one another and is given by

$$S_2^w(\mathbf{x}_1 - \mathbf{x}_2) = \langle I_w(\mathbf{x}_1) I_w(\mathbf{x}_2) \rangle_{\Omega, \Omega}, \quad (27)$$

where  $S_2^w$  is the correlation between two points,  $w$  is the phase index,  $\mathbf{x}_1$  and  $\mathbf{x}_2$  are the locations of points 1 and 2, respectively,  $I_w$  is the binary phase indicator function for the  $w$  phase, and averaging is performed over the entire spatial domain  $\Omega$  [94,95]. The two-point correlation has been found to be useful when describing the microstructure of many materials and porous media and has been used to generate microstructures consistent with experimentally imaged data [94–96].

Because the two-point correlation yields a relationship between the correlation of the pore structure with separation distance but not an exact functional form, an integral measure of the two-point correlation was defined for an isotropic

medium by

$$S_2^{\bar{w}} = \frac{1}{\bar{r}} \int_0^{\bar{r}} S_2^w(r) dr, \quad (28)$$

where  $r$  is the distance between the primary and secondary points of the correlation,  $\bar{r}$  is defined such that

$$\bar{r} = 2r^s, \quad (29)$$

and  $r^s$  is the volume-averaged radius for all spheres comprising the medium.

The anisotropic systems investigated here were generated by transforming an isotropic system of spheres, thus the two-point analysis follows a similar procedure to the isotropic one, with a separate two-point analysis carried out in each dimension, and then transformed by the same scale as the geometry. This generates a vector

$$\mathbf{S}_2^{\bar{w}} = [S_{2x}^{\bar{w}}, S_{2y}^{\bar{w}}, S_{2z}^{\bar{w}}], \quad (30)$$

where  $S_{2x}^{\bar{w}} = S_{2y}^{\bar{w}}$ , and  $S_{2z}^{\bar{w}}$  is transformed by the same factor used to scale the spherical medium into ellipsoids.

An empirical general functional equation of the form

$$\overline{L}_{ii}^w = F(\epsilon^{\bar{w}}, \overline{J}_w^{ws}, \overline{K}_w^{ws}, \overline{R}_{ii}^w, S_{2i}^{\bar{w}}) \quad (31)$$

was evaluated, where the overlines denote nondimensional quantities defined as

$$\overline{J}_w^{ws} = J_w^{ws} d^{\bar{s}}, \quad (32)$$

$$\overline{K}_w^{ws} = K_w^{ws} d^{\bar{s}^2}, \quad (33)$$

$$\overline{R}_{ii}^w = \frac{\epsilon^{\bar{w}^2} \hat{L}_{ii}^w}{d^{\bar{s}^2} \hat{R}_{ii}^w}, \quad (34)$$

$$\overline{L}_{ii}^w = \frac{\hat{L}_{ii}^w}{d^{\bar{s}}}, \quad (35)$$

and the Sauter mean diameter used to derive the nondimensional quantities is

$$d^{\bar{s}} = 6 \frac{(1 - \epsilon^{\bar{w}})}{\epsilon^{\bar{ws}}}, \quad (36)$$

which gives the equivalent diameter of a set of spheres consistent with  $\epsilon^{\bar{w}}$  and  $\epsilon^{\bar{ws}}$ . As a result of nonuniqueness with the nondimensionalization approach taken,  $\epsilon^{\bar{ws}}$  was eliminated from the variable set. The nondimensional form of  $\hat{\mathbf{R}}^w$  was derived by writing in a form equivalent to the standard intrinsic permeability using Eq. (8).

The most general specific functional form evaluated was

$$\overline{L}_{ii}^w = A \epsilon^{\bar{w} \beta_1} \overline{J}_w^{ws \beta_2} \overline{K}_w^{ws \beta_3} \overline{R}_{ii}^w \beta_4 S_{2i}^{\bar{w} \beta_5}, \quad (37)$$

where  $A$  and  $\beta^n$  are empirical coefficients fit based upon nonlinear regression computed based upon the 1000 different systems simulated for Newtonian flow, and simplifications of this general form were also investigated. The estimates for  $\hat{\mathbf{L}}^w$  for each model were compared to those observed in the 10 different 1000-sphere porous medium systems to evaluate the empirical estimates for larger scale systems.

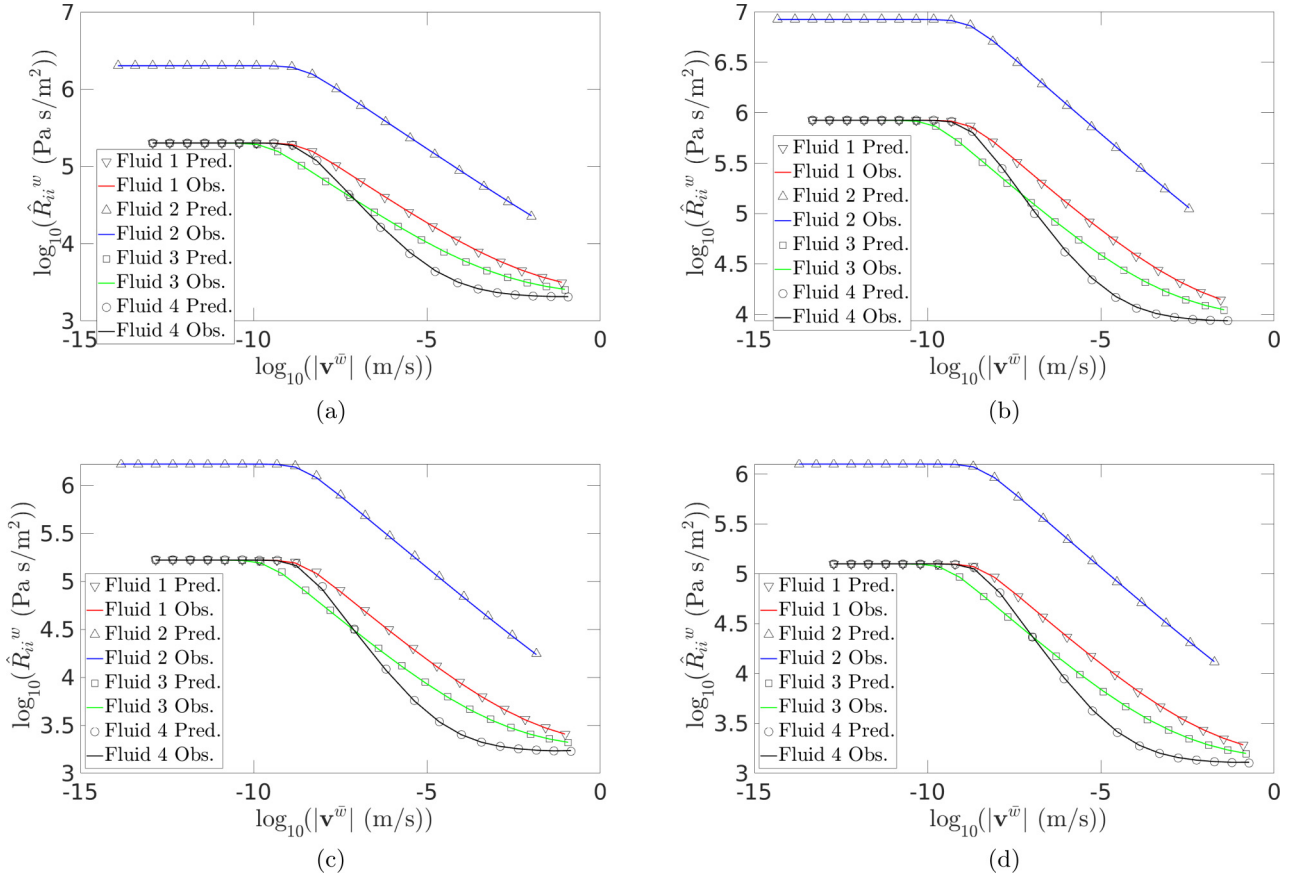


FIG. 2. Comparison of predicted vs observed resistance for: (a) a BCC array of spheres; (b) a random sphere packing with 25 spheres ( $\epsilon^{\bar{w}} = 0.4$ , variance = 0.1); (c) a BCE system in the  $x$  dimension; and (d) a BCE system in the  $z$  dimension.

## V. RESULTS AND DISCUSSION

### A. Macroscale model evaluation and validation

The hydraulic resistance predicted by the macroscale model proposed in Sec. III, using parameters calculated as described in Sec. IV D, was compared to resistances calculated from Eq. (14) for BCC, BCE, and RPSI systems with a log-normal radii variance of 0.1. The comparison was carried out for flow rates that ranged over 10 orders of magnitude in the Stokes regime using the four Carreau fluids described in Sec. IV B, and yielding values of  $\hat{\mathbf{R}}^w$  that spanned nearly three orders of magnitude as shown in Fig. 2. This figure shows the characteristic trend in  $\hat{\mathbf{R}}^w$  in which a transition region exists between the two Newtonian limits. Eq. (22) can be used to quantify the deviation from Newtonian behavior for any value of  $q_i^{\bar{w}}$ . For each flow rate,  $\hat{\mathbf{L}}^w$  was found to vary by less than 1% compared to the Newtonian value, thus the assumption that  $\hat{\mathbf{L}}^w$  is a constant property of the medium is valid for the systems and fluids investigated here as the results obtained are within the numerical accuracy of the simulations.

For each medium, the average relative error in  $\hat{\mathbf{R}}^w$  for each fluid was less than 0.5%, and the maximum relative error observed for fluids 1–3 was 1% and the maximum relative error for fluid 4 was 2% for each medium. For all media, the maximum error in  $\hat{\mathbf{R}}^w$  was observed when the change in resistance from one flow rate to the next was also at its

maximum, near the inflection point in the log of the resistance seen in Fig. 2. The low average and maximum errors in the predicted  $\hat{\mathbf{R}}^w$  for a wide variety of systems and fluids show that the macroscale model presented herein is a valid and useful approximation for a variety of porous medium systems and a range of typical Carreau fluid properties. The error in the macroscale model was most closely related to the rheology of the fluid, and no impact was observed due to medium properties here.

### B. Parameter estimation

While the macroscale model presented in Sec. III was validated for a variety of systems above, this model has thus far required knowledge of microscale quantities to calculate  $\hat{\mathbf{L}}^w$  from Eq. (7) that may not be accessible in many contexts. To investigate approaches that do not require such microscale quantities, several statistical approximations of  $\hat{\mathbf{L}}^w$  based upon more accessible surrogate measures of the porous medium morphology and topology were evaluated.

Statistical functions summarized in Table III were fit to a combined isotropic and anisotropic data set consisting of 1000-sphere and ellipsoid packs. The model fits were carried out in order of complexity, starting with a model with one macroscale parameter, then adding additional parameters. Because it was expected that  $\bar{\mathbf{L}}^w$  and  $\bar{\mathbf{R}}^w$  would be correlated,

TABLE III. Functions fit to porous medium data sets.

| Function | Fitted equation  |
|----------|--|
| 1        | $\overline{L}_{ii}^w = A \overline{R}_{ii}^{w\beta_4}$   |
| 2        | $\overline{L}_{ii}^w = A \epsilon^{\overline{w}\beta_1} \overline{R}_{ii}^{w\beta_4}$  |
| 3        | $\overline{L}_{ii}^w = A \epsilon^{\overline{w}\beta_1} \overline{J}_{w_s}^{w\beta_2} \overline{R}_{ii}^{w\beta_4}$  |
| 4        | $\overline{L}_{ii}^w = A \epsilon^{\overline{w}\beta_1} \overline{J}_{w_s}^{w\beta_2} \overline{K}_{w_s}^{w\beta_3} \overline{R}_{ii}^{w\beta_4}$                              |
| 5        | $\overline{L}_{ii}^w = A \epsilon^{\overline{w}\beta_1} \overline{J}_{w_s}^{w\beta_2} \overline{K}_{w_s}^{w\beta_3} \overline{R}_{ii}^{w\beta_4} \overline{S}_{2r}^{w\beta_5}$ |

each reported fit included  $\overline{R}^w$ . Fits were carried out that excluded  $\overline{R}^w$ , but these fits were of poorer quality than the candidate set shown in Table III and excluded from further consideration. Variables were included in order of accessibility, with  $\overline{R}^w$  being regularly tabulated as permeability, and  $\overline{S}_{2r}^w$  not being tabulated frequently in the literature and requiring microscale data of the pore structure. The parameters determined using a nonlinear least-squares approach are tabulated in Table IV. This table includes the  $R^2$  and generalized cross-validation (GCV) values so that the goodness of fit can be evaluated for each fitted function. Comparison between the observed and predicted values of  $\overline{L}^w$  for select functional fits are depicted in Fig. 3.

The  $R^2$  and GCV values shown in Table IV illustrate that additional variables increased the goodness of fit, but that these increases were modest past the inclusion of  $\overline{R}^w$  and  $\epsilon^{\overline{w}}$ . In particular, the two-point correlation did not increase the goodness of fit significantly relative to the computational burden of calculating it, at least in the form investigated here. This is a similar conclusion to what was found in [97], where two-point correlation was included in a machine-learning algorithm designed to predict permeability. For functions 2–5 in Table IV, the maximum error observed increased for systems that exhibited stochastic variance compared to zero variance media, but did not increase significantly between nonzero variance media. The average relative error observed increased slightly from 4.3% for zero variance media to 5.4% for media with a variance of 0.1, increasing further to 7.7% for the media set with the highest variance. The accuracy of the model was dependent on the variance of the randomly packed media and was not significantly impacted by other medium properties.

The fitted function parameters provided in Table IV allow the calculation of  $\hat{L}$  for a diverse set of porous medium systems with only macroscale system knowledge. In cases where complex microstructure data are available, the models fitted here may be used to generate higher accuracy predictions of  $\hat{L}^w$ ; however, the accuracy of these predictions may not be

much greater than cases where system knowledge is limited to  $\epsilon^{\overline{w}}$ ,  $\epsilon^{\overline{w_s}}$ , and  $\hat{R}^w$ . While posited statistical approximation accuracy based on a diverse data set is an important indicator of a model’s usefulness, it is also important to test such approximations using systems that are of a larger size than the small-scale systems used to derive the approximations due to computational limitations.

C. Statistical function evaluation

To evaluate the statistical function approximations proposed in Sec. VB, a set of simulations were carried out for random packings of 1000 spheres each, with macroscale properties that vary as described in Sec. IV B. These simulations were carried out so that the efficacy of the statistical models of  $\hat{L}^w$  could be evaluated for larger scale systems than those used to derive the approximations. For each medium, simulations were carried out for a single Newtonian fluid flowing through the system, and the  $\hat{L}^w$  was calculated for each system using Eq. (7). This  $\hat{L}^w$  was compared to the  $\hat{L}^w$  predicted using the statistical approximations and their fitted parameters from Tables III and IV, respectively. As an additional validation, one 1000-sphere medium was selected for which a set of simulations were carried out for each fluid described in Table I for a large range of flow rates. The observed resistance from these GNF simulations were compared to the predicted resistances calculated using the analytical resistance model with the statistically predicted  $\hat{L}^w$ .

The average and maximum errors in  $\hat{L}^w$  as predicted by statistical approximations relative to the observed values are tabulated in Table V for several different model functions and porous media. It was found that function 1, which used only hydraulic resistance, was not as accurate as the other functional forms. All the statistical functions were effective at predicting  $\hat{L}^w$  for most media, with relatively large errors when predicting  $\hat{L}^w$  for porous media with the highest variance in the model set. Comparing Tables V and IV, it may be noted that inclusion of curvatures did not significantly increase accuracy compared to the fitted data set, but these quantities significantly increased the accuracy of predicting  $\hat{L}^w$  for the 1000-sphere systems, justifying their inclusion when available. Due to the computational burden of calculating the two-point correlation relative to the increase in accuracy in the fitted data set, function 5 was not included in 1000-sphere evaluation.

The purpose of investigating models for predicting  $\hat{L}^w$  from macroscale quantities is to be able to model flow of non-Newtonian fluids in systems where the microscale averages used in Eq. (7) are not accessible. To evaluate the efficacy of

TABLE IV. Parameter values for functions fit to the combined isotropic and anisotropic media set.

| Function | $R^2$ | GCV                   | $A$   | $\beta_1$ | $\beta_2$ | $\beta_3$ | $\beta_4$ | $\beta_5$ |
|----------|-------|-----------------------|-------|-----------|-----------|-----------|-----------|-----------|
| 1        | 0.709 | $6.46 \times 10^{-3}$ | 3.788 | 0         | 0         | 0         | 0.5567    | 0         |
| 2        | 0.916 | $2.07 \times 10^{-3}$ | 1.108 | -2.824    | 0         | 0         | 0.7679    | 0         |
| 3        | 0.921 | $1.98 \times 10^{-3}$ | 1.151 | -2.892    | -0.2392   | 0         | 0.7776    | 0         |
| 4        | 0.923 | $1.98 \times 10^{-3}$ | 1.141 | -2.893    | -0.2364   | 0.01414   | 0.7792    | 0         |
| 5        | 0.925 | $1.94 \times 10^{-3}$ | 1.099 | -2.774    | -0.2682   | 0.02626   | 0.7639    | -0.0403   |

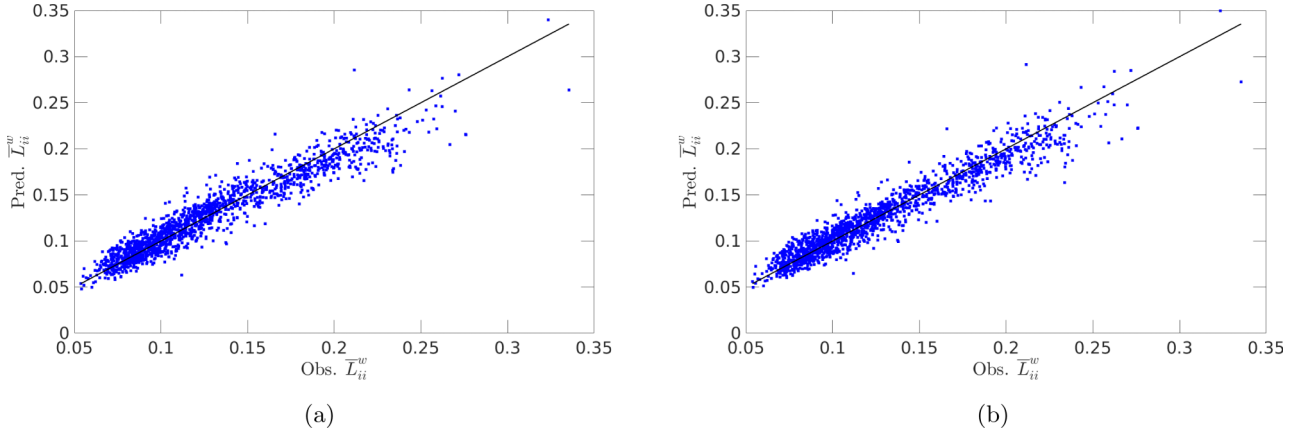


FIG. 3. Comparison of predicted vs observed values for  $\bar{\mathbf{L}}^w$  resulting from nonlinear least squares applied using (a) Function 2 and (b) Function 5.

the statistical approximations when they are applied to such systems, the maximum errors in  $\hat{\mathbf{R}}^w$  calculated from Eq. (15) using the predicted  $\hat{\mathbf{L}}^w$  value relative to the observed  $\hat{\mathbf{R}}^w$  are shown in Table V for all GNFs flowing through a monodisperse, 1000-sphere porous medium. The average relative error in resistance was also tabulated. Additionally, a comparison between the resistance calculated from microscale simulations and the resistance calculated from Eq. (15) using  $\hat{\mathbf{L}}^w$  calculated from using function 2 is presented in Fig. 4.

It has been shown here that it is possible to calculate  $\hat{\mathbf{R}}^w$  analytically from Eq. (15) using parameters that are calculated from the statistical approximation proposed in Sec. VB, without the need to carry out costly microscale simulations or experiments. By calculating  $\hat{\mathbf{L}}^w$  with one of the statistical

approximations from Table III, using model parameters from Table IV, the non-Newtonian resistances of several Carreau model fluids were predicted with an average error of about 1.5% over a range of flow rates that span about 10 orders of magnitude. In particular, statistical function 2 was found to perform very well using only macroscale system parameters that are nearly universally available for porous medium systems. This model may be easily applied to many porous medium systems. As additional computational results become available, further improvements in these results are expected. For example, media with a wider range of porosity would extend the support of the statistical approximations and applicability of the model. It is significant, however, that the flow of a Carreau fluid can be predicted to within roughly the numerical error of the simulations using only a Newtonian characterization of the media and the rheologic properties of a Carreau fluid.

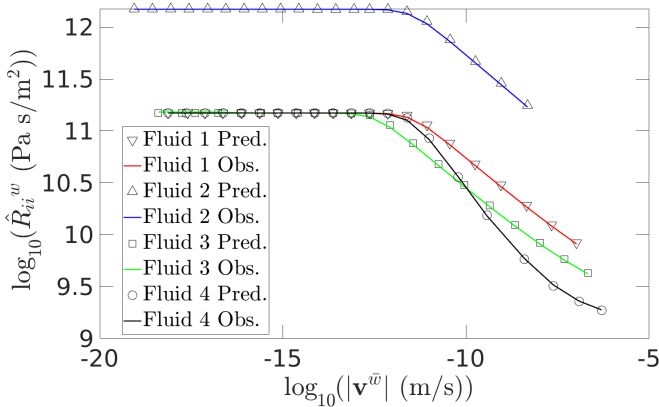


FIG. 4. Comparison of observed resistance and resistance calculated from Eq. (15) using  $\hat{\mathbf{L}}^w$  predicted from model function 2.

## VI. SUMMARY AND CONCLUSIONS

A theoretical development that was recently applied to model the flow of Cross model fluids through porous media [35] was extended and applied to Carreau model fluids, another commonly encountered class of GNF. The accuracy of the posited model was found to be roughly within the bounds of error in the numerical approximations computed for a set of 1000 isotropic and anisotropic porous medium systems.

The Carreau GNF model for flow through a porous medium includes a length-scale tensor  $\hat{\mathbf{L}}^w$ , which has previously been computed based upon microscale simulations of Newtonian flow through a porous medium. To extend the applicability of this work, statistical approximations of  $\hat{\mathbf{L}}^w$

TABLE V. Model error when using statistically fitted functions to predict flow in 1000 sphere (RPSII) system set.

| Function | Average error % in $\hat{\mathbf{L}}^w$ | Maximum error % in $\hat{\mathbf{L}}^w$ | Average error % in $\hat{\mathbf{R}}^w$ | Maximum error % in $\hat{\mathbf{R}}^w$ |
|----------|---|---|---|---|
| 1        | 5.60                                    | 12.3                                    | 1.53                                    | 5.57                                    |
| 2        | 7.69                                    | 14.0                                    | 1.28                                    | 4.80                                    |
| 3        | 4.07                                    | 7.89                                    | 1.35                                    | 5.12                                    |
| 4        | 3.79                                    | 7.09                                    | 1.40                                    | 5.28                                    |

based upon readily available surrogate measures of the pore morphology and topology were posited and evaluated. Results show that the resistance for Carreau flow through a range of media can be predicted *a priori* without microscale simulation data within 2%.

The prediction of  $\hat{\mathbf{L}}^w$  also enables the approximation of Cross-model flows, and potentially other GNF systems, without microscale simulations or experiments.

## ACKNOWLEDGMENTS

This work was supported by Army Research Office Grant No. W911NF1920270, the U.S. Army Engineer Research and Development Center, National Institute of Environmental Health Sciences Grant No. P42ES031007, and National Institute of General Medical Sciences Grant No. R41GM136084. The authors thank W. G. Gray for comments related to the approximation of the length-scale tensor.

- 
- [1] J. A. F. Gerrard, M. F. Perutz, A. Roch, and G. I. Taylor, Measurement of the velocity distribution along a vertical line through a glacier, *Proc. R. Soc. A* **213**, 546 (1952).
- [2] C. Ancey and M. Meunier, Estimating bulk rheological properties of flowing snow avalanches from field data, *J. Geophys. Res.* **109** (2004).
- [3] C. Ancey, Plasticity and geophysical flows: A review, *J. Non-Newtonian Fluid Mech.* **142**, 4 (2007).
- [4] A. C. Barr, R. T. Pappalardo, and S. Zhong, Convective instability in ice I with non-Newtonian rheology: Application to the icy Galilean satellites, *J. Geophys. Res.* **109** (2004).
- [5] G. Hulme, The interpretation of lava flow morphology, *Geophys. J. Intl.* **39**, 361 (1974).
- [6] Y. S. Wu, An approximate analytical solution for non-Darcy flow toward a well in fractured media, *Water Resour. Res.* **38**, 5 (2002).
- [7] I. Sonder, B. Zimanowski, and R. Buttner, Non-Newtonian viscosity of basaltic magma, *Geophys. Res. Lett.* **33**, 2005GL024240 (2006).
- [8] E. Lev, M. Spiegelman, R. J. Wysocki, and J. A. Karson, Investigating lava flow rheology using video analysis and numerical flow models, *J. Volcanol. Geotherm. Res.* **247–248**, 62 (2012).
- [9] M. Peyrounette, Y. Davit, M. Quintard, and S. Lorthois, Multiscale modelling of blood flow in cerebral microcirculation: Details at capillary scale control accuracy at the level of the cortex, *PLoS ONE* **13**, e0189474 (2018).
- [10] N. Bessonov, A. Sequira, S. Simakov, Y. Vassilevskii, and V. Volpert, Methods of blood flow modelling, *Math. Model. Nat. Phenom.* **11**, 1 (2016).
- [11] K. Sriram, M. Intaglietta, and D. M. Tartakovsky, Non-Newtonian flow of blood in arterioles: Consequences for wall shear stress measurements, *Microcirculation* **21**, 628 (2014).
- [12] S. Chakraborty, Dynamics of capillary flow of blood into a microfluidic channel, *Lab Chip* **5**, 421 (2005).
- [13] M. G. Rabby, A. Razzak, and M. M. Molla, Pulsatile non-Newtonian blood flow through a model of arterial stenosis, *Procedia Eng.* **56**, 225 (2013).
- [14] F. Zami-Pierre, R. de Loubens, M. Quintard, and Y. Davit, Effect of disorder in the pore-scale structure on the flow of shear-thinning fluids through porous media, *J. Non-Newtonian Fluid Mech.* **261**, 99 (2018).
- [15] A. A. Osipov, Fluid mechanics of hydraulic fracturing: A review, *J. Petrol. Sci. Eng.* **156**, 513 (2017).
- [16] W. Norman, R. Jasinski, and E. Nelson, Hydraulic fracturing process and compositions, U.S. Patent No. 5,551,516 (1996).
- [17] R. Barati and J.-T. Liang, A review of fracturing fluid systems used for hydraulic fracturing of oil and gas wells, *J. Appl. Polym. Sci.* **131**, app.40735 (2014).
- [18] M. Zhang, M. Prodanovic, M. Mirabolghasemi, and J. Zhao, 3D microscale flow simulation of shear-thinning fluids in a rough fracture, *Transp. Porous Media* **128**, 243 (2019).
- [19] A. C. Barbati, J. Desroches, A. Robisson, and G. H. McKinley, Complex fluids and hydraulic fracturing, *Annu. Rev. Chem. Biomol. Eng.* **7**, 415 (2016).
- [20] C. Xie, W. Lv, and M. Wang, Shear-thinning or shear-thickening fluid for better EOR?—A direct pore-scale study, *J. Petrol. Sci. Eng.* **161**, 683 (2018).
- [21] C. L. Perrin, P. M. J. Tardy, K. S. Sorbie, and J. C. Crawshaw, Experimental and modeling study of Newtonian and non-Newtonian fluid flow in pore network micromodels, *J. Colloid Interface Sci.* **295**, 542 (2006).
- [22] T. C. Buchley and D. L. Lord, What to learn about hydraulic fracturing fluids, *Oil Gas J.* **71**, 84 (1973).
- [23] J. R. A. Pearson and P. M. J. Tardy, Models for flow of non-Newtonian and complex fluids through porous media, *J. Non-Newtonian Fluid Mech.* **102**, 447 (2002).
- [24] K. S. Sorbie, P. J. Clifford, and E. R. W. Jones, The rheology of pseudoplastic fluids in porous media using network modeling, *J. Colloid Interface Sci.* **130**, 508 (1989).
- [25] S. Liu and J. H. Masliyah, Non-linear flows in porous media, *J. Non-Newtonian Fluid Mech.* **86**, 229 (1999).
- [26] T. Sochi, Non-Newtonian flow in porous media, *Polymer* **51**, 5007 (2010).
- [27] T. Tosco, D. L. Marchisio, F. Lince, and R. Sethi, Extension of the Darcy-Forchheimer law for shear-thinning fluids and validation via pore-scale flow simulations, *Transp. Porous Media* **96**, 1 (2013).
- [28] A. Rodríguez de Castro and M. Agnaou, Numerical investigation of the apparent viscosity dependence on Darcy velocity during the flow of shear-thinning fluids in porous media, *Transp. Porous Media* **129**, 93 (2019).
- [29] C. N. Basset, M. R. Abou Najm, A. Ammar, R. D. Stewart, S. C. Hauswirth, and G. Saad, Physically based model for extracting dual-permeability parameters using non-Newtonian fluids, *Vadose Zone J.* **18**, 1 (2019).
- [30] S. C. Hauswirth, M. R. Abou Najm, and C. T. Miller, Characterization of the pore structure of porous media using non-Newtonian fluids, *Water Resour. Res.* **55**, 7182 (2019).
- [31] A. Rodríguez de Castro and B. Goyeau, A pore network modelling approach to investigate the interplay between local and Darcy viscosities during the flow of shear-thinning fluids in porous media, *J. Colloid Interface Sci.* **590**, 446 (2021).
- [32] A. Skelland, *Non-Newtonian Flow and Heat Transfer* (John Wiley and Sons, New York, 1967).

- [33] F. A. Morrison, *Understanding Rheology* (Oxford University Press, Oxford, 2001).
- [34] R. B. Bird, W. E. Stewart, and E. N. Lightfoot, *Transport Phenomena*, 2nd ed. (Wiley, New York, 2002).
- [35] C. A. Bowers and C. T. Miller, Generalized Newtonian fluid flow in porous media, *Phys. Rev. Fluids* **6**, 123302 (2021).
- [36] S. C. Hauswirth, C. A. Bowers, C. P. Fowler, P. B. Schultz, A. Dye Hauswirth, T. M. Weigand, and C. T. Miller, Modeling Cross model non-Newtonian fluid flow in porous media, *J. Contam. Hydrol.* **235**, 103708 (2020).
- [37] W. G. Gray and C. T. Miller, *Introduction to the Thermodynamically Constrained Averaging Theory for Porous Medium Systems* (Springer, Cham, 2014).
- [38] P. D. M. Spelt, T. Selerland, C. J. Lawrence, and P. D. Lee, Flows of inelastic non-Newtonian fluids through arrays of aligned cylinders. Part 1. Creeping flows, *J. Eng. Math.* **51**, 57 (2005).
- [39] P. Coussot, Yield stress fluid flows: A review of experimental data, *J. Non-Newtonian Fluid Mech.* **211**, 31 (2014).
- [40] D. Bauer, L. Talon, Y. Peysson, H. B. Ly, G. Batot, T. Chevalier, and M. Fleury, Experimental and numerical determination of Darcy's law for yield stress fluids in porous media, *Phys. Rev. Fluids* **4**, 063301 (2019).
- [41] H. E. Fayed, N. A. Sheikh, and O. Iliev, On laminar flow of non-Newtonian fluids in porous media, *Transp. Porous Media* **111**, 253 (2016).
- [42] A. R. de Castro, Extending Darcy's law to the flow of yield stress fluids in packed beds: Method and experiments, *Adv. Water Resour.* **126**, 55 (2019).
- [43] A. R. Castro and G. Radilla, Non-Darcian flow of shear-thinning fluids through packed beads: Experiments and predictions using Forchheimer's law and Ergun's equation, *Adv. Water Resour.* **100**, 35 (2017).
- [44] N. Kaur, R. Singh, and R. K. Wanchoo, Flow of Newtonian and non-Newtonian fluids through packed beds: An experimental study, *Transp. Porous Media* **90**, 655 (2011).
- [45] F. Zami-Pierre, R. de Loubens, M. Quintard, and Y. Davit, Transition in the flow of power-law fluids through isotropic porous media, *Phys. Rev. Lett.* **117**, 074502 (2016).
- [46] D. V. Boger, Demonstration of upper and lower Newtonian fluid behavior in a pseudoplastic fluid, *Nature (London)* **265**, 126 (1977).
- [47] V. Subbaraman, R. A. Mashelkar, and J. Ulbrecht, Extrapolation procedures for zero shear viscosity with a falling sphere viscometer, *Rheol. Acta* **10**, 429 (1971).
- [48] R. P. Chhabra and P. H. T. Uhlherr, Estimation of zero-shear viscosity of polymer solutions from falling sphere data, *Rheol. Acta* **18**, 593 (1979).
- [49] Q. Xiong, T. G. Baychev, and A. P. Jivkov, Review of pore network modelling of porous media: Experimental characterisations, network constructions and applications to reactive transport, *J. Contam. Hydrol.* **192**, 101 (2016).
- [50] T. Sweijen, S. M. Hassanizadeh, B. Chareyre, and L. Zhuang, Dynamic pore-scale model of drainage in granular porous media: The pore-unit assembly method, *Water Resour. Res.* **54**, 4193 (2018).
- [51] H. Adloo and B. Abbasi, Some insights into the use of pore network simulations for predicting single-phase fluid flow in model porous media, *Microfluidics Nanofluidics* **25**, 61 (2021).
- [52] S. Chen, X. He, V. Bertola, and M. Wang, Electro-osmosis of non-Newtonian fluids in porous media using lattice Poisson–Boltzmann method, *J. Colloid Interface Sci.* **436**, 186 (2014).
- [53] A. Yoshino, Y. Hotta, T. Hirozane, and M. Endo, A numerical method for incompressible non-Newtonian fluid flows based on the lattice Boltzmann method, *J. Non-Newtonian Fluid Mech.* **147**, 69 (2007).
- [54] S. P. Sullivan, L. F. Gladden, and M. L. Johns, Simulation of power-law fluid flow through porous media using lattice Boltzmann techniques, *J. Non-Newtonian Fluid Mech.* **133**, 91 (2006).
- [55] D. Kehrwald, Lattice Boltzmann simulation of shear-thinning fluids, *J. Stat. Phys.* **121**, 223 (2005).
- [56] E. Aharonov and D. H. Rothman, Non-Newtonian flow (through porous-media)—A lattice-Boltzmann method, *Geophys. Res. Lett.* **20**, 679 (1993).
- [57] L. Orgéas, C. Geindreau, J. L. Auriault, and J. F. Bloch, Upscaling the flow of generalised Newtonian fluids through anisotropic porous media, *J. Non-Newtonian Fluid Mech.* **145**, 15 (2007).
- [58] L. Orgeas, Z. Idris, C. Geindreau, J.-F. Bloch, and J.-L. Auriault, Modelling the flow of power-law fluids through anisotropic porous media at low-pore Reynolds number, *Chem. Eng. Sci.* **61**, 4490 (2006).
- [59] J. K. Woods, P. D. M. Spelt, P. D. Lee, T. Selerland, and C. J. Lawrence, Creeping flows of power-law fluids through periodic arrays of elliptical cylinders, *J. Non-Newtonian Fluid Mech.* **111**, 211 (2003).
- [60] L. Patacchini and R. de Loubens, A class of physically stable non-linear models of flow through anisotropic porous media, *Transp. Porous Media* **97**, 409 (2013).
- [61] T. J. Sadowshi and R. B. Bird, Non-Newtonian flow through porous media I. Theoretical, *Trans. Soc. Rheol.* **9**, 243 (1965).
- [62] G. Chauveteau, Rodlike polymer solution flow through fine pores: Influence of pore size on rheological behavior, *J. Rheol.* **26**, 111 (1982).
- [63] R. Parnas and Y. Cohen, Power-law fluids in porous media, *Chem. Eng. Commun.* **53**, 3 (1987).
- [64] R. E. Hayes, A. Afacan, B. Boulanger, and A. V. Shenoy, Modelling the flow of power law fluids in a packed bed using a volume-averaged equation of motion, *Transp. Porous Media* **23**, 175 (1996).
- [65] S. Berg and J. Wunnik, Shear rate determination from pore-scale flow fields, *Transp. Porous Media* **117**, 229 (2017).
- [66] N. Zamani, I. Bondino, R. Kaufmann, and A. Skauge, Computation of polymer in-situ rheology using direct numerical simulation, *J. Petrol. Sci. Eng.* **159**, 92 (2017).
- [67] J. Bear, *Dynamics of Fluids in Porous Media* (Elsevier, New York, 1972).
- [68] G. de Marsily, *Quantitative Hydrogeology: Groundwater Hydrology for Engineers* (Academic Press, San Diego, 1986).
- [69] W. G. Gray and C. T. Miller, Thermodynamically constrained averaging theory approach for modeling flow and transport phenomena in porous medium systems: 3. Single-fluid-phase flow, *Adv. Water Resour.* **29**, 1745 (2006).
- [70] C. T. Miller and W. G. Gray, Thermodynamically constrained averaging theory approach for modeling flow and transport phenomena in porous medium systems: 2. Foundation, *Adv. Water Resour.* **28**, 181 (2005).

- [71] W. G. Gray and C. T. Miller, TCAT analysis of capillary pressure in non-equilibrium, two-fluid-phase, porous medium systems, *Adv. Water Resour.* **34**, 770 (2011).
- [72] W. G. Gray and C. T. Miller, A generalization of averaging theorems for porous medium analysis, *Adv. Water Resour.* **62**, 227 (2013).
- [73] W. G. Gray and C. T. Miller, Thermodynamically constrained averaging theory approach for modeling flow and transport phenomena in porous medium systems: 1. Motivation and overview, *Adv. Water Resour.* **28**, 161 (2005).
- [74] C. T. Miller and W. G. Gray, Thermodynamically constrained averaging theory approach for modeling flow and transport phenomena in porous medium systems: 4. Species transport fundamentals, *Adv. Water Resour.* **31**, 577 (2008).
- [75] W. G. Gray and C. T. Miller, Thermodynamically constrained averaging theory approach for modeling flow and transport phenomena in porous medium systems: 5. Single-fluid-phase transport, *Adv. Water Resour.* **32**, 681 (2009).
- [76] W. G. Gray and C. T. Miller, Thermodynamically constrained averaging theory approach for modeling flow and transport phenomena in porous medium systems: 7. Single-phase megascale flow models, *Adv. Water Resour.* **32**, 1121 (2009).
- [77] A. S. Jackson, C. T. Miller, and W. G. Gray, Thermodynamically constrained averaging theory approach for modeling flow and transport phenomena in porous medium systems: 6. Two-fluid-phase flow, *Adv. Water Resour.* **32**, 779 (2009).
- [78] W. G. Gray, A. L. Dye, J. E. McClure, L. J. Pyrak-Nolte, and C. T. Miller, On the dynamics and kinematics of two-fluid-phase flow in porous media, *Water Resour. Res.* **51**, 5365 (2015).
- [79] I. V. Rybak, W. G. Gray, and C. T. Miller, Modeling two-fluid-phase flow and species transport in porous media, *J. Hydrol.* **521**, 565 (2015).
- [80] G. Sciumé, S. E. Shelton, W. G. Gray, C. T. Miller, F. Hussain, M. Ferrari, P. Decuzzi, and B. A. Schrefler, Tumor growth modeling from the perspective of multiphase porous media mechanics, *Mol. Cell. Biomech.* **9**, 193 (2012).
- [81] G. Sciumé, S. Shelton, W. G. Gray, C. T. Miller, F. Hussain, M. Ferrari, P. Decuzzi, and B. A. Schrefler, A multiphase model for three-dimensional tumor growth, *New J. Phys.* **15**, 015005 (2013).
- [82] C. T. Miller, W. G. Gray, and B. A. Schrefler, A continuum mechanical framework for modeling tumor growth and treatment in two- and three-phase systems, *Arch. Appl. Mech.* **92**, 461 (2021).
- [83] C. T. Miller, W. G. Gray, C. E. Kees, I. V. Rybak, and B. J. Shepherd, Modelling sediment transport in three-phase surface water systems, *J. Hydraul. Res.* **57**, 439 (2019).
- [84] S. R. Williams and A. P. Philipse, Random packings of spheres and spherocylinders simulated by mechanical contraction, *Phys. Rev. E* **67**, 051301 (2003).
- [85] C. Greenshields, *OpenFOAM User Guide version 6* (OpenFOAM Foundation, 2018).
- [86] M. Icardi, G. Boccardo, D. L. Marchisio, T. Tosco, and R. Sethi, Pore-scale simulation of fluid flow and solute dispersion in three-dimensional porous media, *Phys. Rev. E* **90**, 013032 (2014).
- [87] C. Pan, M. Hilpert, and C. T. Miller, Pore-scale modeling of saturated permeabilities in random sphere packings, *Phys. Rev. E* **64**, 066702 (2001).
- [88] L. S. Caretto, A. D. Gosman, S. V. Patankar, and D. B. Spalding, Two calculation procedures for steady, three-dimensional flows with recirculation, *Proc. Third Intl. Conf. Numer. Methods Fluid Mech.* **19**, 60 (1972).
- [89] J. E. McClure, R. T. Armstrong, M. A. Berrill, S. Schlüter, S. Berg, W. G. Gray, and C. T. Miller, Geometric state function for two-fluid flow in porous media, *Phys. Rev. Fluids* **3**, 084306 (2018).
- [90] C. T. Miller, K. Bruning, C. L. Talbot, J. E. McClure, and W. G. Gray, Nonhysteretic capillary pressure in two-fluid porous media: Definition, evaluation, validation, and dynamics, *Water Resour. Res.* **55**, 6825 (2019).
- [91] C. Sun, J. E. McClure, P. Mostaghimi, A. L. Herring, D. E. Meisenheimer, D. Wildenschild, S. Berg, and R. T. Armstrong, Characterization of wetting using topological principles, *J. Colloid Interface Sci.* **578**, 106 (2020).
- [92] R. T. Armstrong, J. E. McClure, V. Robins, Z. Liu, C. H. Arns, S. Schlüter, and S. Berg, Porous media characterization using Minkowski functionals: Theories, applications, and future directions, *Transp. Porous Med.* **130**, 305 (2019).
- [93] W. G. Gray, K. Bruning, and C. T. Miller, Non-hysteretic functional form of capillary pressure in porous media, *J. Hydraul. Res.* **57**, 747 (2019).
- [94] Y. Jiao, F. H. Stillinger, and S. Torquato, Modeling heterogeneous materials via two-point correlation functions. II. Algorithmic details and applications, *Phys. Rev. E* **77**, 031135 (2008).
- [95] C. J. Gommers, Y. Jiao, and S. Torquato, Microstructural degeneracy associated with a two-point correlation function and its information content, *Phys. Rev. E* **85**, 051140 (2012).
- [96] M. V. Karsanina, K. M. Gerke, E. B. Skvortsova, and D. Mallants, Universal spatial correlation functions for describing and reconstructing soil microstructure, *PLoS ONE* **10**, e0126515 (2015).
- [97] B. Prifling, M. Röding, P. Townsend, M. Neumann, and V. Schmidt, Large-scale statistical learning for mass transport prediction in porous materials using 90,000 artificially generated microstructures, *Front. Materials* **8**, 786502 (2021).